

1 **Morphology of Mitochondria in Spatially Restricted Axons Revealed by Cryo-**
2 **Electron Tomography**

3

4 Tara D. Fischer^{1,2†}, Pramod K. Dash^{1,3}, Jun Liu^{1,‡}, and M. Neal Waxham^{1*}

5

6 **Author Affiliations:**

7 ¹Department of Neurobiology and Anatomy, McGovern Medical School, University of
8 Texas Health Science Center at Houston, Houston, TX 77030

9

10 ²The University of Texas MD Anderson Cancer Center UTHealth Graduate School of
11 Biomedical Sciences; The University of Texas Health Science Center at Houston,
12 Houston, Texas 77030

13

14 ³Vivian L. Smith Department of Neurosurgery, McGovern Medical School, University of
15 Texas Health Science Center at Houston, Houston, TX 77030

16

17

18 Present Address:

19 [†]Biochemistry Section, Surgical Neurology Branch, National Institute of Neurological
20 Disorders and Stroke, National Institutes of Health, Bethesda, MD 20892

21 [‡]Department of Microbial Pathogenesis & Microbial Sciences Institute, Yale School of
22 Medicine, New Haven, CT 06519

23

24 ***Corresponding Author:** M. Neal Waxham. 6431 Fannin St., MSB 7.254, Houston, TX
25 77030. (713) 500-5621. m.n.waxham@uth.tmc.edu

26

27 **Keywords:** Cryo-electron tomography, mitochondria, mitochondrial transport,
28 mitochondrial membranes

29

30

31

32 **Abstract**

33 Neurons project axons to local and distal sites and can display heterogeneous
34 morphologies with limited physical dimensions that may influence the structure of large
35 organelles such as mitochondria. Using cryo-electron tomography (cryo-ET), we
36 characterized native environments within axons and presynaptic varicosities to examine
37 whether spatial restrictions within these compartments influence the morphology of
38 mitochondria. Segmented tomographic reconstructions revealed distinctive
39 morphological characteristics of mitochondria residing at the narrowed boundary
40 between presynaptic varicosities and axons with limited physical dimensions (~80 nm),
41 compared to mitochondria in non-spatially restricted environments. Furthermore,
42 segmentation of the tomograms revealed discrete organizations between the inner and
43 outer membranes, suggesting possible independent remodeling of each membrane in
44 mitochondria at spatially restricted axonal/varicosity boundaries. Thus, cryo-ET of
45 mitochondria within axonal subcompartments reveals that spatial restrictions do not
46 obstruct mitochondria from residing within them but limited available space can influence
47 their gross morphology and the organization of the inner and outer membranes. These
48 findings offer new perspectives on the influence of physical and spatial characteristics of
49 cellular environments on mitochondrial morphology and highlights the potential for
50 remarkable structural plasticity of mitochondria to adapt to spatial restrictions within
51 axons.

52

53 Introduction

54 Neurons are architecturally complex cells that can extend axonal projections with
55 elaborate arborization for several hundreds of millimeters (and in some cases, meters) to
56 form synaptic connections with local and distal targets [1-3]. Depending on the target,
57 presynaptic compartments can either be found at the end of axons (terminal boutons) or
58 tracking along axons as intermediate swellings (*en passant* boutons or varicosities),
59 such as in the unmyelinated CA3->CA1 axons of the hippocampus [3-7]. The bead-like
60 presynaptic varicosities are morphologically heterogeneous, displaying diameters that
61 can range from 1-2 μm connected by thin axon segments that can have diameters less
62 than 100 nm [4, 5, 8, 9].

63 Tracking through the axons is a well-developed system of microtubules that
64 mediate motor-driven anterograde and retrograde transport of signaling cargoes, protein
65 complexes and organelles critical for function and homeostasis at distant synapses [10,
66 11]. Transport of these intracellular components creates a spatially and temporally
67 dynamic environment within the axon that can contain a variety of organelles and
68 cargoes of different shapes, sizes, and number [12, 13]. As axon segments
69 interconnecting varicosities can be remarkably thin and occupied by various structures,
70 whether physical adaptations to available space are required for the motility of large
71 organelles, such as mitochondria, with diameters ranging between 100-500 nm, poses
72 an interesting question [14, 15]. Mitochondria within axons and synaptic compartments
73 are particularly critical for development, function, and plasticity. During transport,
74 mitochondria are known to make frequent stops, or saltatory movements, at presynaptic
75 compartments to provide local ATP synthesis and calcium regulation required for proper
76 neurotransmission [16-20]. Given the morphological complexity of axons, restricted
77 physical dimensions and available space could potentially influence the subcellular
78 localization, distribution, and transport of mitochondria required to meet local energy
79 needs and for supporting synaptic transmission. Although mitochondria are
80 morphologically dynamic organelles that can exist in a variety of shapes and sizes, how
81 mitochondria adapt to the physical constraints presented in axons has not been
82 previously examined.

83 Advances in microscopy and imaging techniques have played a pivotal role in
84 revealing the three-dimensional architecture of neurons and their intracellular
85 environments at resolutions reaching the nanometer scale [21, 22]. In the current study,
86 we employed cryo-electron tomography (cryo-ET) to visualize three-dimensional spatial

87 relationships and organellar structure within cultured hippocampal axons and
88 varicosities. The unique native state preservation afforded by cryopreservation and the
89 resolution of cryo-ET revealed that axon morphology and physically restrictive
90 intracellular dimensions present a previously unrecognized influence on the morphology
91 and ultrastructure of mitochondria residing at the boundary between large varicosities
92 and small axonal subcompartments.

93

94 **Results**

95 **Preparation of primary hippocampal neurons for cryo-ET**

96 Primary neuronal cultures from E18 rat hippocampi were grown on holey carbon
97 grids prior to cryo-preservation. At 10 days post plating, primary hippocampal neurons
98 have extended dendritic and axonal processes and have established presynaptic
99 varicosities and initial excitatory synaptic connections [23]. **Figure 1A** and **B** show
100 representative bright field images of neurons cultured on a Quantifoil grid where
101 widespread elaboration of processes is evident. **Figure 1C** and **D** demonstrate images
102 of companion grids that were fixed and immunolabeled with antibodies to
103 calcium/calmodulin dependent protein kinase II alpha (CaMKII α) and synapsin 1 to
104 visualize the excitatory neuron population and presynaptic varicosities, respectively.
105 CaMKII α antibodies largely label soma and processes, while the synapsin 1 antibody
106 shows distinct puncta representing enrichment of synaptic vesicles at presynaptic
107 varicosities.

108 For cryo-ET, fiducial gold markers were applied to prepared grids to aid in image
109 alignment during data acquisition and image processing, and then cryopreserved by
110 plunge freezing in liquid ethane. Cryopreservation conserves the near native state of the
111 preparation permitting an assessment of spatial relationships between organelles
112 present in different neuronal compartments free of fixation- or stain-induced artifacts.
113 Low magnification images were first collected (**Fig. 1E**) and montaged to provide maps
114 for targeting areas of interest for data collection. A higher magnification image reveals
115 the distribution of presynaptic varicosities and axonal processes (**Fig. 1F**). Varicosities
116 and axons can be seen residing on both the carbon and overlying the grid holes. To
117 provide maximum contrast, tomographic data collection was targeted to cryopreserved
118 structures within the grid holes. In these preparations, the increased thickness of the
119 soma and proximal dendrites prevented sufficient electron beam penetration for imaging
120 of these structures. In contrast, the sample thickness surrounding the axonal processes

121 and varicosities was ideal, permitting a detailed assessment of the spatial relationships
122 of cytoskeletal structures and organelles within these subcompartments.

123

124 **Organelle populations of presynaptic varicosities in primary hippocampal neurons**
125 **are heterogeneous**

126 Areas were randomly chosen, and tilt series were collected from varicosities and
127 axon segments overlying grid holes to visualize cytoskeletal and organellar structures.
128 **Figure 2A** shows a slice through a representative tomographic reconstruction with
129 various resident organelles and structures visible, including two mitochondria, a multi-
130 vesicular body (MVB), microtubules, endoplasmic reticulum (ER) and a collection of
131 vesicles. Supplementary **Figure S1** shows 2D images of identified organelles and other
132 structures observed within the population of varicosities analyzed. To determine the
133 three-dimensional (3D) relationship between the different structures, segmentation was
134 accomplished of the tomographic reconstruction of both the presynaptic varicosity and
135 the adjoining axon (**Fig. 2B; Movie S1**). The reconstruction demonstrates microtubules
136 (light blue) forming a continuous set of tracks traveling from one end of the varicosity to
137 the other. Microtubules are well organized and relatively straight in axons, however, they
138 exhibit greater curvature in the varicosity, while again gathering together and
139 straightening when passing through the adjoining axon segment. The ER (yellow) also
140 forms a reticulated and continuous structure spanning the entire length of the varicosity,
141 consistent with other reports on the ubiquitous presence of ER in axons and synaptic
142 terminals [21]. Mitochondria, MVB, and other sac-like compartments, exhibit more
143 random distributions within the varicosity, while vesicles appeared to be somewhat
144 clustered. To determine if the presence of each of these identifiable organelles was
145 consistent across varicosities, we analyzed their distribution and characteristics in an
146 additional 77 tomographic reconstructions. ER and microtubules were present in 100%
147 of presynaptic varicosities, vesicles were present in 97%, mitochondria in 82%, sac-like
148 compartments in 38%, MVBs in 21%, lamellar bodies in 9%, and autophagosomes in 4%
149 (Table 1).

150

Table 1. Organelle population representations

	Presence within population (%) n = 77
Mitochondria	81.8
Number/Varicosity	
0	18.1

1	66.2
>1	15.5
Gross Morphology	
Round	26.3
Slightly Tubular	30.2
Tubular	43.4
Internal Morphology	
Thin, tubulated	23.6
Thick, unstructured	76.3
Endoplasmic Reticulum	100
Contact with Mito	38.4
Near Mito	89.7
Vesicles	97.4
Number/Cell	
1-25	2.5
25-50	64.9
50-100	10.3
>100	6.4
MVBs	20.7
Lamellar Bodies	9.0
Unidentified Membrane-bound	37.6
Compartments	
Autophagosome	38.9

151

152 Variations in distinct sub-features of the observed organelle populations also
153 emerged in 3D at high resolution. Specifically, the ubiquitous ER was observed in close
154 apposition to almost every other organelle within the varicosities, consistent with ER-
155 membrane contact sites described by others [21]. The vesicular population was
156 heterogeneous in number, ranging from 1 to >100 vesicles per varicosity. 75% of
157 varicosities contained <50 vesicles, 10% had 50-100, and 6% contained more than 100
158 (Table 1). Vesicles were observed in clusters with electron-dense filamentous
159 connections (data not shown), consistent with previous reports of proteinaceous
160 (synapsin, Bassoon, and/or ERC2) tethering of synaptic vesicles [12, 13]. Mitochondrial
161 cristae structure within the 3D tomographic datasets was variable, but could be broadly
162 segregated into two distinct populations based on ultrastructural features (**Fig. S2**). A
163 population of mitochondria displayed the canonical thin, tubular cristae morphology (**Fig.**
164 **S2A**), while a second population displayed thick, unstructured cristae (**Fig. S2B**).

165 In contrast to the heterogeneous appearance and distribution of organelles in
166 presynaptic varicosities, the adjoining axonal segments were more consistent in
167 composition. The most obvious components were microtubules that were seen as
168 continuous elements, gathered at the sites of axonal narrowing at both ends of the

169 varicosity. Microtubules did not display variability in diameter (~20 nm), however they
170 did vary in number among different processes and occupied a significant portion of the
171 available volume within the axon. As noted, microtubules are the essential tracks
172 required for motor driven organelle transport and are critical for maintaining synaptic
173 homeostasis and neuronal signaling. The corresponding microtubule occupation of
174 axonal space leaves the qualitative impression that the available volume in axons to
175 accommodate large organelles, such as mitochondria, might be an under-appreciated
176 constraint affecting transport. The magnitude of this spatial constraint can be visually
177 appreciated in **Movie S2**.

178

179 **Mitochondria display distinct morphological features at spatially restricted** 180 **axon/varicosity boundaries**

181 Previous EM studies have reported an average axonal diameter between 0.08
182 and 0.4 μm for unmyelinated cortical axons and an average varicosity diameter of ~1-2
183 μm [1, 5, 7, 8]. Varicosities and axons in our cryopreserved hippocampal preparations
184 exhibited slightly smaller Feret diameters, with an average of 649 and 81 nm for
185 varicosities and axons, respectively (Table 2). Additionally, the average Feret diameter
186 of mitochondria observed in hippocampal varicosities was ~250 nm. These dimensions
187 (summarized in **Table 2**) further reinforce the idea that significant spatial constraints
188 exist that may influence mitochondrial structure in axons.

189

Table 2. Two-dimensional morphological measures

	n	Average	Range
Varicosity			
Diameter	200	649 \pm 241 nm	257 nm – 1.65 μm
Axon			
Diameter	195	81 \pm 27 nm	33 – 204 nm
Mitochondria			
Length	67	647 \pm 305 nm	255 nm – 1.68 μm
Diameter	71	291 \pm 87 nm	160 – 547 nm

190

191 For more in-depth investigation of this issue, high magnification tomographic data
192 were collected targeting mitochondria residing at the boundary where the varicosity
193 narrows into the small axonal segment. While such precise mitochondrial positioning
194 was rare in the cryo-preserved neuronal population, the static events that were captured
195 revealed distinct mitochondrial morphologies at the boundaries between varicosities and

196 axons. **Movie S3** and **S4** demonstrate a mitochondrion partially residing in both a
197 neuronal varicosity and the adjoining axon segment among the other organelles
198 occupying space in these compartments. The portion of the mitochondrion residing in
199 the varicosity is 305 nm in Feret diameter, while the portion of the mitochondrion residing
200 in the axonal segment is narrowed to only 70 nm in diameter at its tip. Thus, the
201 mitochondrion displays a major morphological change with an approximately 77%
202 reduction in diameter within the axon. **Figure 3A** shows a snapshot of the segmented
203 mitochondrion as well as additional examples of mitochondria captured at the
204 varicosity/axonal boundary (**Fig. 3B and C**). **Figure 3C** shows a reconstruction that
205 revealed two mitochondria residing in the varicosity and adjoining axon segment, with a
206 portion of a third residing mainly in the axon. **Movies S3 – S10** demonstrate several
207 tomographic reconstructions of mitochondria displaying similar morphologies at the
208 varicosity/axon boundary. **Figure 4** and **Movie S9** show a particularly revealing
209 example, in which a mitochondrion was captured bridging a short (100 nm in length)
210 axon segment between two varicosities. The short narrow space produced a barbell
211 shaped mitochondrion with a diameter between 200-300 nm in both varicosities while
212 the portion spanning the axon segment was only 19 nm in diameter. To illustrate the
213 ultrastructural features of the mitochondrion spanning the two varicosities, the inner
214 mitochondrial membrane (IMM) and cristae were segmented in addition to the outer
215 membrane (OMM; **Fig. 4C**). The resolution of this tomographic reconstruction was not
216 sufficient to determine whether the IMM was continuous through the short axon
217 segment, however **Movie S10** demonstrates an additional example of a mitochondrion
218 spanning a short axon segment between two varicosities, in which the IMM appears
219 continuous in the constricted section of the axon. Analysis of eight mitochondria
220 exhibiting these drastic morphological features revealed an average of 84% ($n = 8$, $SD =$
221 6%) reduction in the Feret diameter of the mitochondrial area in the varicosity relative to
222 the adjoining axon segment. These captured events highlight the potential adaptability
223 of mitochondrial morphology to accommodate the available space within an axon. Note
224 that in all of the segmented tomographic reconstructions in **Figure 3 and 4**, the
225 presence of microtubules and additional organelles, such as the ER, further restricts the
226 available volume to mitochondria within axons.

227

228 **Mitochondrial membranes display unique organizations within spatially restrictive**
229 **axons**

230 Mitochondrial ultrastructure is thought to be dynamic with remodeling of the inner
231 membrane and formation of specified subcompartments, termed cristae [24-26]. Given
232 the atypical gross morphologies of mitochondria we observed between varicosities and
233 the adjoining axonal segments, we questioned if the inner mitochondrial membrane also
234 displays distinct structural features in axons with limited physical dimensions. To
235 address this issue, the outer and inner membranes of mitochondria captured at the
236 boundary between varicosities and adjoining axons were segmented, separating the
237 outer membrane, and two regional components of the IMM, the inner boundary
238 membrane (IBM) and the cristae. A conservative approach was taken during manual
239 segmentation of cristae (i.e., only clearly discernible cristae membranes were included).
240 Segmentation of each of these mitochondrial components revealed discrete
241 morphologies between the inner and outer membranes. Most notably, two distinctions
242 were observed between the outer membrane and the adjacent IBM at the narrowed
243 mitochondrial tip in the adjoining axon segment. First, in some instances the IBM was
244 observed to maintain apposition to the outer membrane at the narrowed mitochondrial
245 tip entering the axon (**Fig. 5A**). Both the inner (orange) and outer (green) membranes
246 can be seen narrowing as they enter the restricted axonal space. Interestingly, cristae
247 (pink) are largely absent from this narrowed portion of the mitochondrion (~69 nm in
248 diameter) residing in the axon. Second, the outer membrane was observed to separate
249 from the inner membrane, leaving a space free of the inner membrane and matrix of the
250 mitochondrion (**Fig. 5B**). Thus, it appears the IMM does not always remain in apposition
251 with the OMM within the rather dramatic tubulation evident of the outer membrane
252 residing within the restricted space of the axon. Two out of the eight representations of
253 mitochondria displaying these atypical morphological features in our dataset also show
254 the OMM separated from the IMM. **Movie S11** shows the segmented model of the three
255 mitochondria in **Figure 3C and 5C**. The left mitochondrion can be seen to display the
256 OMM separated from the IMM, while the right mitochondrion displays the OMM and IMM
257 in juxtaposition, demonstrating the occurrence of both events in one varicosity/axon
258 boundary area.

259

260 Discussion

261 Although the transport of mitochondria within axons has been widely studied, the
262 potential morphological adaptation of these large organelles to restricted physical
263 dimensions and available space within axons has not been discussed [18, 27, 28]. The

264 current study provides insight into spatial environments within presynaptic varicosities
265 and thin axons of cryopreserved hippocampal neurons, unperturbed by fixation or stains
266 via 3D cryo-ET. Distinct morphological characteristics of mitochondria were revealed at
267 the boundaries between large varicosities and axon segments with limited physical
268 dimensions (~ 80 nm). To our knowledge, this is the first study to describe such atypical
269 mitochondrial morphologies apparently influenced by the limitations of physical space
270 within thin axons. Additionally, the 3D reconstruction and segmentation of mitochondrial
271 ultrastructure revealed distinct morphological features between the inner and outer
272 mitochondrial membranes at spatially restricted axonal/varicosity boundaries, suggesting
273 possible differential regulation of each membrane during these morphological
274 adaptations.

275 Axon morphology can be widely variable depending on brain region. *En passant*
276 boutons are common in axons of the hippocampus and cortex, giving rise to
277 heterogeneous axon morphologies with presynaptic varicosities distributed along thin
278 unmyelinated axons [3-7]. As axons and synaptic varicosities are dynamic,
279 heterogeneous environments that can be occupied by organelles and molecules differing
280 in size and number, it is important to consider whether available space within the axon
281 may constrain motility or transport of large cargo, such as mitochondria. Using the
282 advantages of cryo-ET, we were able to capture the static spatial environments in thin
283 axons and presynaptic varicosities of cultured hippocampal neurons to examine
284 organelle characteristics and distribution. Mitochondria, in particular, at an average of
285 250 nm in diameter, presented a clear spatial challenge to inhabit axons that are, on
286 average, three times smaller (~80 nm). In the 3D segmentation of mitochondria residing
287 at the boundary between the larger presynaptic varicosity and thin adjoining axon
288 segments, we observed mitochondria displaying atypical morphological features.
289 Mitochondria displayed a normal morphology within the varicosity and a narrowed
290 tubulated portion, creating a “tip” that existed in the narrowed space within the axon.
291 Interestingly, in some cases this narrowed portion of the mitochondrion was smaller than
292 the inner boundary of the axonal plasma membrane, suggesting that additional material,
293 not apparent in the tomograms, might further constrain the available space within the
294 axon. The ability of mitochondria to display morphological diameters near 20 nm when
295 challenged with limiting available space within axons is surprising and suggests
296 mitochondrial morphology may be more adaptable in nature than previously considered.
297 While it is important to emphasize that our methodology does not address temporal

298 dynamics of mitochondria within axons, these observations highlight the potential for the
299 adaptability of mitochondrial morphology and present interesting questions to the
300 mechanisms that may be involved.

301 Movement of Intracellular cargo and transport within axons is mediated by
302 microtubule-associated motor proteins that create the driving force necessary to pull
303 organelles through the cytoplasm in axons and varicosities [11, 28]. Specifically, kinesin
304 and dynein motor proteins exert a mechanical force on the mitochondrion to drive
305 polarity-directed movement within axons through interactions with outer mitochondrial
306 membrane and adaptor proteins, such as Miro and Milton [29]. We speculate that
307 directional forces induced by motor proteins may drive the morphological features of the
308 mitochondrial membrane, as observed in the current study. Kinesins, in particular, are
309 known to induce membrane deformation or tubulation in *in vitro* reconstituted
310 membranes [30, 31]. A recent study also described similar thin tubulation of
311 mitochondria that is mediated by KIF5B, a member of the kinesin family [32].
312 Interestingly, the influence of mechanical forces on mitochondrial membrane dynamics
313 was recently demonstrated by the recruitment of mitochondrial fission machinery and
314 subsequent division at sites of induced physical constriction [33]. In fact, it is also
315 possible that recruitment of such machinery would lead to the production of fission
316 intermediates of the mitochondria of reduced size that would facilitate their movement
317 through axons. If so, appropriate machinery would have to be present in adjacent
318 varicosities for the reassembly of mitochondria. Although the distinct morphological
319 features of mitochondria in axons observed in our static, cryopreserved tomographic
320 reconstructions cannot address dynamics for transport, whether force-driven microtubule
321 interactions play a role is an interesting possibility. Additionally, it is also possible that
322 neuronal activity might influence the structure of varicosities, axons or mitochondria that
323 would impact the magnitude of this problem. In this context, a recent report analyzing
324 varicosities and axons in hippocampal slices, showed that high-frequency stimulation of
325 axons, increased the size of varicosities and axons [34], although the peak effects on
326 size were relatively modest (~5% increase in varicosity/axonal diameter). Thus, further
327 investigation into the precise mechanisms involved in the regulation of space within
328 axons and mitochondrial morphological adaptations within the available space is
329 warranted.

330 Mitochondrial function is highly dependent on the unique architecture of the inner
331 mitochondrial membrane (IMM), in which the respiratory complexes along with ATP

332 synthase are concentrated in formations of distinct compartments, termed cristae [26,
333 35-37]. Classic and more recent studies examining inner membrane morphology and
334 cristae formation have shown distinct ultrastructural features in states of high cellular
335 energy demands, however whether inner membrane structure changes occur
336 correspondingly with gross morphological changes (excluding those involved in
337 mitochondrial fission or fusion) is not well defined [24-26, 38-41]. Therefore, we
338 questioned whether the significant reduction in size of mitochondria within the physically
339 restrictive axonal space also affected their internal structure. Segmentation of cristae
340 and the inner boundary membrane (IBM), distinct components of the IMM, revealed
341 intriguing differences in the relationship between internal structure and the outer
342 mitochondrial membrane (OMM). In some cases, the IBM remained in close apposition
343 with the OMM at the narrowed tip of the mitochondrion in the axon. Interestingly, this
344 area was also void of cristae, whereas cristae structure remained unperturbed in the
345 portion of the mitochondrion that resided in the varicosity, suggesting possible
346 differential regulation of cristae compartments with adaptation to the limited space within
347 axons. Conversely, a few mitochondria displayed a dissociation of the inner and outer
348 mitochondrial membrane, in which the outer membrane was no longer in apposition with
349 the IBM, but distinctly separated in the narrowed tip of the mitochondrion creating a
350 “matrix-free” space. The IBM and cristae remained intact and unperturbed within the
351 portion of the mitochondrion residing in the varicosity. The visualization of the 3D
352 ultrastructure of mitochondria displaying these morphological features within spatially
353 restricted axons suggests a potentially new instance of structural remodeling of the IMM.
354 Mechanistically, this observation generates several interesting questions to the
355 regulation and dynamic nature of mitochondrial ultrastructure, as well as the functional
356 status of mitochondria in different axonal compartments. Although mechanisms for
357 regulating inner membrane morphology remain incompletely defined, recent research
358 has provided insight into some mechanisms involved in the regulation of cristae structure
359 and IMM morphology [25, 37, 42, 43]. In addition to Opa1, the primary IMM fusion
360 protein, ATP synthase and the mitochondrial contact site and cristae organizing system
361 (MICOS) exhibit membrane bending functions and are proposed to determine curvature
362 of the cristae membrane [37, 38]. MICOS components have also been implicated in
363 regulating cristae morphology, as well as inner-outer membrane tethering, which could
364 be a potential mechanism driving the differences in inner-outer membrane apposition or
365 dissociation observed in the present study [44, 45]. Moreover, distinct events of IMM

366 constriction independent from the OMM have also recently been observed that are
367 driven by increased mitochondrial matrix calcium levels [46-48]. Thus, there is some
368 evidence at the cellular level for differential morphological regulation of the inner and
369 outer membranes. The 3D reconstructions of the OMM, IBM, and cristae in the cryo-
370 preserved axon, and the observed dissociation between membrane morphologies in the
371 current study lends support for the notion that the OMM and IMM can be remodeled
372 independently. Functionally, the observed changes in cristae and IMM morphology also
373 pose the question as to whether the lack of cristae or adaptation of the IMM influence
374 the functional capacity of these mitochondria. Although the technical limitations of
375 measuring mitochondrial function in relation to mitochondrial structure are challenging,
376 these will be critical investigations in uncovering the dynamic and adaptive nature of the
377 IMM and regulation of mitochondrial function in axons.

378 The importance of mitochondrial dynamics and synaptic localization to support
379 neuronal function is well recognized (for reviews see [17, 18, 49]). Mitochondria must
380 traffic through axons and populate distal synapses to mitigate local energy depletion and
381 maintain calcium homeostasis required for vesicle release and recycling [16, 50, 51].
382 Additionally, mitochondria undergo active fission, fusion, mitophagy, and maintain
383 contact with other organelles to communicate, functionally adapt, and maintain quality
384 control within the local environment. Thus, disruptions in mitochondrial motility and
385 dynamic behaviors can be detrimental to synaptic communication, plasticity, and
386 survival, and have been implicated in several neurodegenerative processes (reviewed in
387 [17, 29, 52]). The current study highlights the potential implications for spatial
388 restrictions dictated by axon morphology to influence mitochondrial morphology, and
389 potentially motility within the axon. These findings offer new perspectives on the physical
390 and spatial influence of the cellular environment on mitochondrial morphology and
391 highlights the remarkable structural plasticity of mitochondria to adapt to the limited
392 available space within axons. Given the importance of membrane structure for
393 mitochondrial function and the necessary transport of mitochondria for maintaining
394 synaptic health and neurotransmission, these findings have far reaching implications for
395 mitochondrial and neuronal biology. Future research will be essential to gain
396 mechanistic insight to regulation of structural changes at mitochondrial membranes and
397 the influence of morphological adaptations of mitochondria during axonal transport.

398

399

400

401

402

403

404

405

406

407

408

409 **Materials and Methods**

410

411 Neuronal Culture and Cryopreservation

412 Primary neuronal cultures were prepared from E18 rat hippocampi. All protocols
413 involving vertebrate animals were approved by the Institutional Animal Care and Use
414 Committee prior to initiating the studies. Briefly, pooled hippocampi were digested with
415 papain for 20 min at 37°C and then triturated with a 10 ml pipet. Cells were counted and
416 diluted in Opti-MEM containing 20 mM glucose to a density of 1.5×10^5 /ml. 200 mesh
417 gold grids covered with Quantifoil 2/1 carbon were placed in 35 mm glass bottom Mat-
418 Tek dishes and were treated overnight with 100 ug/ml poly-D-lysine. The dishes were
419 then washed 3x with sterile water before plating cells at a density of 1.5×10^6 /dish. After
420 letting the cells attach for 1 hr at 37°C/5%CO₂, the media was exchanged for Neurobasal
421 A supplemented with 2% B-27 (Life Technologies), GlutaMAX (Thermo Scientific,
422 Waltham, CA), and penicillin-streptomycin (Sigma, St. Louis, MO) and incubated for 10 d
423 at 37°C/5%CO₂.

424 To cryopreserve intact neurons, the grids were lifted from the Mat-Tek dishes
425 and 5 uL of Neurobasal media containing BSA coated 10 nm gold fiducials was applied.
426 Fiducial gold facilitates tracking during image acquisition of tilt series and alignment of
427 image frames during post-acquisition processing. After manual blotting, the grids were
428 plunged into liquid ethane cooled with liquid N₂. The entire process between removal of
429 the grid from the culture dish and plunge freezing was on average ~30 s, but never more
430 than 60 s. Cryo-preserved grids were stored in liquid N₂ until use.

431

432 Immunocytochemistry

433 Immunostaining of neurons grown on Quantifoil grids was accomplished by fixing
434 the neurons at 10 d post-plating in freshly prepared 4% paraformaldehyde in 0.1 M
435 phosphate buffer, pH 7.4, for 10 min at room temperature. The fixative was removed
436 and reaction quenched with a 5 min incubation in 50 mM glycine in 0.1 M phosphate
437 buffer, pH 7.4. Neurons were permeabilized with 0.5% TX-100 in 0.1 M phosphate
438 buffer, pH 7.4, for 15 min and then non-specific sites blocked with Blocking buffer (2%
439 normal goat serum, 1% bovine serum albumin, 0.1% TX-100 in 0.1 M phosphate buffer,
440 pH 7.4) for 30 min. Primary antibodies were diluted 1:1000 in Blocking buffer and
441 incubated for 1 hr at room temp. Primary antibodies included a monoclonal antibody to
442 CaMKII α (created in our lab; [53]) and a rabbit polyclonal antibody to synapsin 1
443 (Synaptic Systems Inc.). Grids were then washed 3x, 5 min each, with Wash buffer
444 (0.2% normal goat serum, 0.1% bovine serum albumin, 0.01% TX-100 in 0.1 M
445 phosphate buffer, pH 7.4). Grids were then incubated in 1:500 dilution of Alexa 488
446 labeled goat anti-mouse IgG and Alexa 568 labeled goat anti-rabbit IgG diluted in
447 Blocking buffer for 30 min at room temperature. Grids were washed 3x 5 min each in
448 Wash buffer, once in 0.1 M phosphate buffer, pH 7.4 and then mounted in Fluoromount
449 anti-fade mounting compound. Bright field and fluorescent images were collected with a
450 10x, or 40x magnification using a 0.9 NA water immersion lens on a Zeiss inverted
451 microscope using an Andor Zyla 4.0 CMOS camera. Exposure time, shutter and filter
452 wheel (Sutter Instrument Co.) were controlled through Metamorph software (Molecular
453 Devices).

454

455 Cryo-electron Tomography

456 For tomographic data collection, single-axis tilt series were collected from -50° to
457 $+50^\circ$ in 3° increments at approximately $-8 \mu\text{m}$ under focus on an FEI Polara G2 operated
458 at 300 kV equipped with a Gatan K2 Summit direct electron detector operated in photon
459 counting mode. Data collection was performed in a semi-automated fashion using Serial
460 EM software operated in low-dose mode [54]. Briefly, areas of interest were identified
461 visually and 8×8 montages were collected at low magnification (2400x) and then
462 individual points were marked for automated data collection. Data were collected at
463 either 8.5 or 4.5 $\text{\AA}/\text{pixel}$. Movies of 8-10 dose-fractionated frames were collected at each
464 tilt angle and the electron dose spread across all images was limited to a total dose of $<$
465 $100 \text{ e}^-/\text{\AA}^2$ per tilt series. There is a “missing wedge” of information in the reconstructions
466 due to the inability to collect tilt series through a full 180° ($\pm 90^\circ$) of stage tilting.

467 Additionally, as the stage is tilted the electron path through the sample increases,
468 decreasing the contrast and quality of the high tilt images. For our system, tilting the
469 stage +/- 50° was found to be an optimal compromise. The missing wedge leads to
470 anisotropic resolution producing elongation and blurring in the Z-dimension and
471 tomographic reconstructions need interpreted acknowledging this limitation.

472

473 Tomographic Reconstruction and Segmentation

474 Each tomographic data set was drift corrected with MotionCorr2 [55] and stacks
475 were rebuilt and then aligned using IMOD [56, 57]. Tomograms of the aligned stacks
476 were then reconstructed using TOMO3D [58, 59]. Contrast was enhanced using SIRT
477 reconstruction implemented in TOMO3D.

478 Reconstructed tomograms were further processed using the median, non-local
479 means, and Lanczos filters in Amira (FEI, ThermoFisher Scientific) for manual and semi-
480 automated segmentation. Segmentation was accomplished by manually tracing
481 membranes for each Z slice of the tomographic data set. Membranes were identified and
482 segmented with reference to visualization in all three dimensions (X, Y, and Z). The
483 brush tool was primarily used in manual segmentation. When possible, masking
484 approaches were also used in combination with density thresholding for semi-automated
485 segmentation. After segmentation, smoothing tools were employed for the manual
486 tracings and surfaces were rendered for model construction. All measurements (length
487 and diameter) were performed in either Amira using the 3D measurement tool or in
488 IMOD.

489

490 Acknowledgements

491 The authors would like to acknowledge Dr. Andrey Tsvetkov, Ndidi Uzor and Felix
492 Moruno Manchon for help with primary neuronal cultures. We would also like to thank
493 Dr. Michael Beierlein, Dr. Richard Youle and Dr. Matt Swulius for advice on the
494 manuscript. This study was supported by grants from the National Institute of
495 Health/National Institute of Neurological Disease and Stroke; R01NS101686 (MWN and
496 PKD), R01NS087149 (PKD) and F31NS098790, Ruth L. Kirchstein National Research
497 Service Award Predoctoral Fellowship (TF). PKD acknowledges support from the Nina
498 and Michael Zilkha endowment and MNW acknowledges support from the William
499 Wheless III professorship. The Polara electron microscope was supported, in part,

500 through the Structural Biology Imaging Center at UTHSC—Houston. The Gatan K2
501 Summit was funded by the National Institutes of Health—Award S10OD016279.

502 **Figure Legends**

503

504 Figure 1. Growth and characterization of primary hippocampal neurons on EM grids.
505 Hippocampal neurons were isolated from E18 rats and plated on poly-D-lysine coated
506 Quantifoil 2/1 gold grids. A) Low magnification bright field image showing the typical
507 distribution of neuronal soma and processes after 10 d in culture. B) Higher
508 magnification image of the area from the white box in panel (A) with neuronal processes
509 highlighted by white brackets. (C) Wide-field fluorescence image showing
510 immunolabeling of the neuron specific protein CaMKII α in green and the presynaptic
511 vesicle associated protein synapsin 1 in red. The blue color is from a bright field overlay
512 of the same area that also highlights the bars of the EM grid. (D) Higher magnification
513 image in a different area of the same immunolabeled grid highlighting the punctate
514 staining of synapsin I (red; arrowheads) along processes typical of *en passant*
515 varicosities in hippocampal axons. Blue is again from where the grid bars and holes in
516 the Quantifoil grid are apparent. Scale bars in panels A-C = 100 μm and in panel D = 50
517 μm . (E) Low magnification montage of one area in a cryopreserved grid of hippocampal
518 neurons 10 d post-plating showing the typical distribution of axons and synaptic
519 varicosities. Scale bar = 10 μm . F) Higher magnification representation from (E; white
520 box) showing the axon and varicosity distribution overlying carbon (slightly darker areas)
521 and grid holes. Examples of varicosities lying within grid holes are marked with white
522 asterisks while examples lying on the carbon are marked with red asterisks. Axon
523 segments interconnecting the varicosities are highlighted with black brackets. Scale bar
524 = 2 μm .

525

526 Figure 2. Tomographic reconstruction of a typical pre-synaptic varicosity and adjoining
527 axon segment. A) 2D slice from the tomographic reconstruction showing the distribution
528 of organelles in the varicosity PM: plasma membrane, MT: microtubules, Mito:
529 mitochondrion, ER: endoplasmic reticulum, Ves: vesicle, MVB: multi-vesicular body.
530 Scale bar = 200 nm. B) Segmented representation of the entire 3D tomogram volume
531 shown in (A) revealing the relative size and spatial distribution of the organelle
532 environment in the varicosity and axon segment. Plasma membrane (dark blue),
533 microtubules (light blue), mitochondrial outer membrane (dark green), endoplasmic
534 reticulum (yellow), vesicles (dark purple), multi-vesicular body (light purple), unidentified
535 membrane-bound compartment (pink). Scale bar = 200 nm.

536

537 Figure 3. Mitochondria display atypical morphological features in physically restrictive
538 axons. A-C) Three different 3D segmented reconstructions showing representative
539 examples of mitochondria residing partially in the varicosity and adjoining axon
540 segments, demonstrating different morphological states at the transition from the
541 varicosity into the restricted space of the axon segment. Additional organelles
542 occupying the axon space are also segmented. For ease of visualization, not all of the
543 organelles and structures in the varicosity are shown. The plasma membrane (dark
544 blue), microtubules (light blue), mitochondrial outer membrane (dark green),
545 endoplasmic reticulum (yellow), vesicles (dark purple) are highlighted.

546

547 Figure 4. Structural features of a mitochondrion captured spanning two varicosities. A)
548 10 nm slice through a 3D tomographic reconstruction showing a mitochondrion spanning
549 two closely spaced varicosities connected by a short (~100 nm) axon segment. An
550 expanded region of the red box shown in (A) reveals the tubulated nature of the portion
551 of the mitochondrion within the axon segment. Microtubules can be seen running
552 parallel to the tubulated portion of the mitochondrion. B) shows a surface rendered
553 version highlighting the plasma membrane (purple), microtubules (blue) small segment
554 of ER (yellow) and mitochondria (green). C) is the same mitochondrion as in (B)
555 displaying distinct segmentation of the outer membrane (green), inner membrane
556 (orange), and cristae (pink).

557

558 Figure 5. Mitochondrial membranes display distinct morphological features at the
559 boundaries of varicosities and axons with limited physical dimensions. A-C) To highlight
560 the membrane organization of the mitochondria shown in Figure 3A-C, the cristae and
561 inner and outer membranes of the 3D reconstructions were segmented. A) Mitochondrial
562 inner and outer membranes remain in close apposition within the narrowed portion of
563 this mitochondrion resident in the axon. B) Mitochondrial outer membrane is separated
564 from the inner membrane, creating a distinct “matrix-free” compartment in this portion of
565 the mitochondria residing in the axon. C) Three mitochondria near the varicosity/axon
566 junction show distinct internal membrane organization. The left mitochondrion shows a
567 portion of outer membrane separated from inner membrane while the top right
568 mitochondrion is narrowed near the axon junction, but the inner and outer membranes
569 remain in apposition. A short tip of a third mitochondrion is partially captured at the edge

570 of the tomogram that also shows inner and outer membranes together. Plasma
571 membrane (dark blue), mitochondrial outer membrane (dark green), mitochondrial inner
572 boundary membrane (orange), cristae (pink).

573

574

575 Supporting Figure Legends

576

577 Figure S1. 2D images from tomographic reconstructions of different membrane bound
578 organelles observed in the varicosities of cryopreserved hippocampal neurons. A)
579 mitochondrion, B) MVB and vesicles (arrowheads). C) ER and an unidentified
580 membrane-bound compartment (arrowhead), D) Autophagosome, E) Lamellar body.
581 Scale bar = 200 nm.

582

583 Figure S2. Different populations of mitochondrial cristae ultrastructures in varicosities. A)
584 Representations of mitochondria displaying thin, tubulated cristae. B) Representations of
585 mitochondria displaying thick, unstructured cristae. Populations were identified based on
586 full 3D tomographic reconstructions. Scale bar = 200 nm.

587

588 Movie S1. Animation of the 3D tomographic reconstruction and overlay of the
589 segmented structures in Figure 2. Scale bar = 200 nm.

590

591 Movie S2. Animation demonstrating space within an axon encountered by a
592 mitochondrion presented in the X dimension. 3D tomographic reconstruction
593 corresponds to Figure 3B and 5B. Scale bar = 200 nm.

594

595 Movie S3. Animation of the 3D tomographic reconstruction and overlay of the
596 segmented structures in Figure 3A. 3D tomographic reconstruction also corresponds to
597 Figure 5A. Scale bar = 200 nm.

598

599 Movie S4. Movie of the tilt series of tomographic data set corresponding to Figure 3A
600 and 5A. Scale bar = 200 nm.

601

602 Movie S5. Movie of the 3D tomographic reconstruction corresponding to Figure 3B and
603 5B. Scale bar = 200 nm.

604

605 Movie S6. Movie of the tilt series of tomographic data set corresponding to Figure 3C
606 and 5C. Scale bar = 200 nm.

607

608 Movie S7. Movie of a mitochondrion at spatially restricted axonal/varicosity boundary.
609 Scale bar = 200 nm.

610

611 Movie S8. Movie of an additional mitochondrion at spatially restricted axonal/varicosity
612 boundary. Scale bar = 200 nm.

613

614 Movie S9. Movie of the 3D tomographic reconstruction corresponding to Figure 4. Scale
615 bar = 200 nm.

616

617 Movie S10. Movie of a 3D tomographic reconstruction displaying a mitochondrion
618 spanning a short axon segment and residing in two varicosities. Scale bar = 200 nm.

619

620 Movie S11. Animation of the 3D tomographic reconstruction and overlay of the
621 segmented membranes of mitochondria in Figure 3D. Scale bar = 200 nm.

622

623 References

624

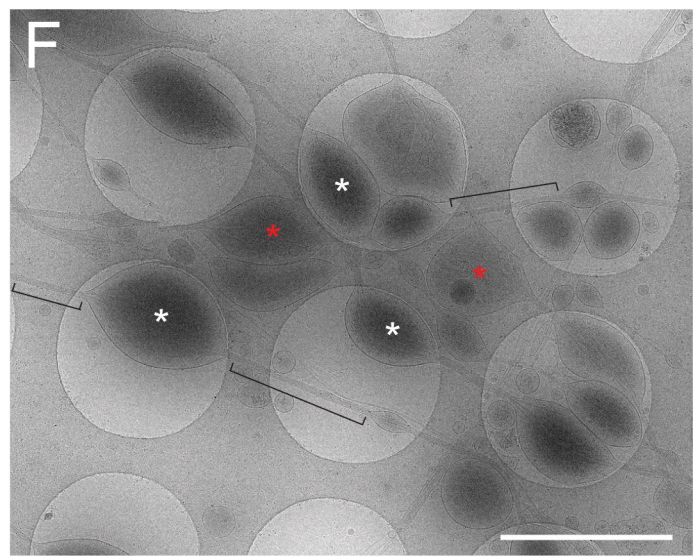
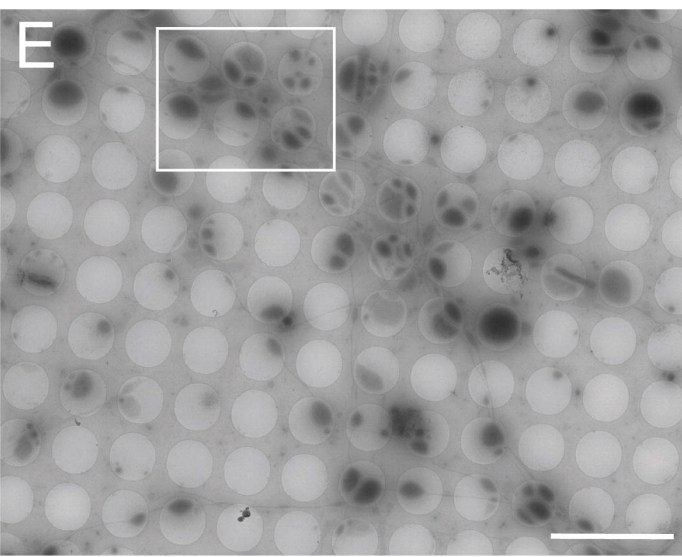
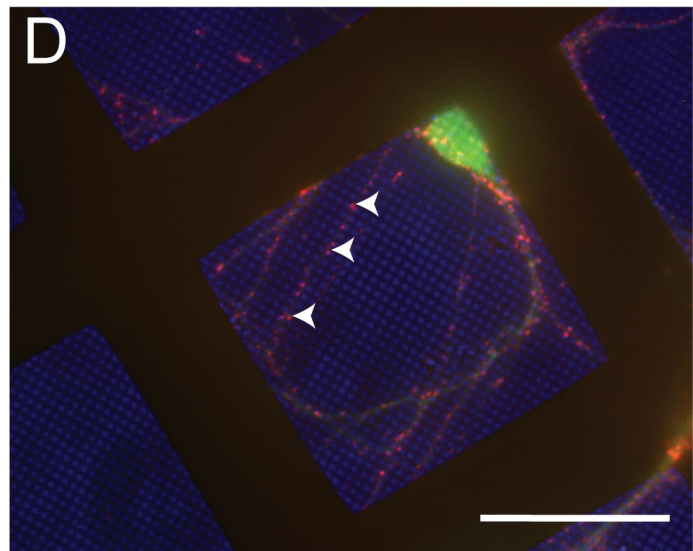
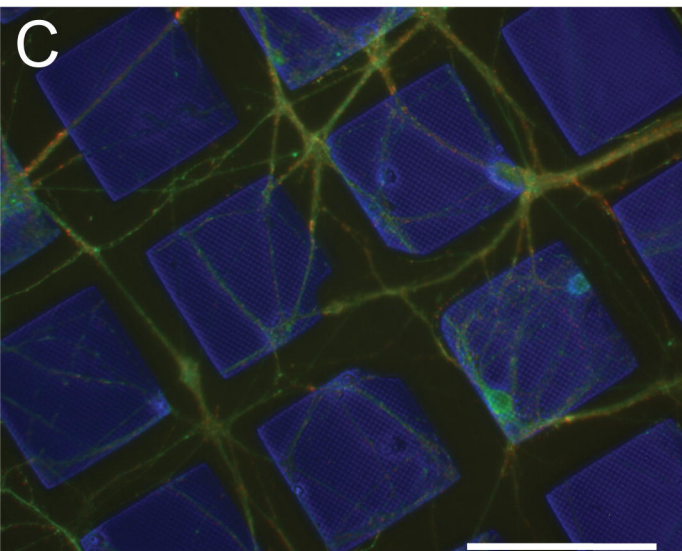
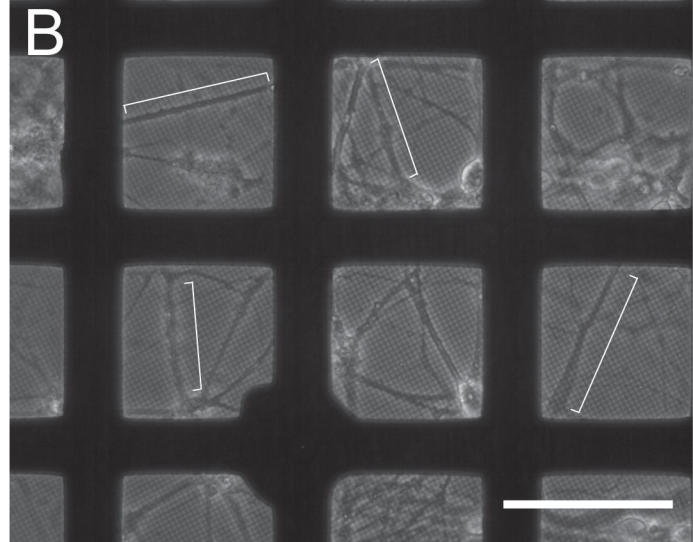
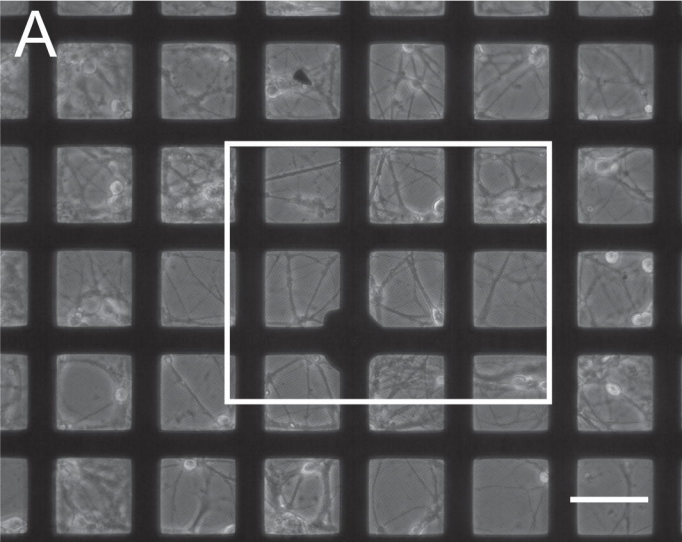
- 625 1. Debanne D. Information processing in the axon. *Nature Reviews Neuroscience*.
626 2004;5:304-16. doi: 10.1038/nrn1397. PubMed PMID: 15034555.
- 627 2. Ishizuka N, Weber J, Amaral DG. Organization of intrahippocampal projections
628 originating from CA3 pyramidal cells in the rat. *The Journal of Comparative*
629 *Neurology*. 1990;295:580-623. doi: 10.1002/cne.902950407. PubMed PMID:
630 2358523.
- 631 3. Li X-G, Somogyi P, Ylinen A, Buzsáki G. The hippocampal CA3 network: An in
632 vivo intracellular labeling study. *Journal of Comparative Neurology*.
633 1994;339:181-208. doi: 10.1002/cne.903390204. PubMed PMID: 8300905.
- 634 4. Shepherd GM, Harris KM. Three-dimensional structure and composition of CA3--
635 >CA1 axons in rat hippocampal slices: implications for presynaptic connectivity
636 and compartmentalization. *J Neurosci*. 1998;18(20):8300-10. PubMed PMID:
637 9763474.
- 638 5. Westrum LE, Blackstad TW. An electron microscopic study of the stratum
639 radiatum of the rat hippocampus (regio superior, CA 1) with particular emphasis
640 on synaptology. *J Comp Neurol*. 1962;119:281-309. PubMed PMID: 14000149.
- 641 6. Muller D, Nikonenko I. Dynamic presynaptic varicosities: A role in activity-
642 dependent synaptogenesis. *Trends in Neurosciences*. 2003;26:573-5. doi:
643 10.1016/j.tins.2003.08.010. PubMed PMID: 14585594.
- 644 7. Shepherd GMG, Raastad M, Andersen P. General and variable features of
645 varicosity spacing along unmyelinated axons in the hippocampus and
646 cerebellum. *Proceedings of the National Academy of Sciences*. 2002;99:6340-5.
647 doi: 10.1073/pnas.052151299. PubMed PMID: 11972022.
- 648 8. Berbel P, Innocenti GM. The development of the corpus callosum in cats: a light-
649 and electron-microscopic study. *J Comp Neurol*. 1988;276(1):132-56. doi:
650 10.1002/cne.902760109. PubMed PMID: 3192762.
- 651 9. Anderson JC, Martin KAC. Does bouton morphology optimize axon length?
652 *Nature Neuroscience*. 2001;4:1166-7. doi: 10.1038/nn772. PubMed PMID:
653 11713473.
- 654 10. Conde C, Cáceres A. Microtubule assembly, organization and dynamics in axons
655 and dendrites. *Nature Reviews Neuroscience*. 2009;10:319-32. doi:
656 10.1038/nrn2631. PubMed PMID: 19377501.
- 657 11. Saxton WM, Hollenbeck PJ. The axonal transport of mitochondria. *Journal of Cell*
658 *Science*. 2012;125:2095-104. doi: 10.1242/jcs.053850. PubMed PMID:
659 22619228.
- 660 12. Fernández-Busnadiego R, Schrod N, Kochovski Z, Asano S, Vanhecke D,
661 Baumeister W, et al. Insights into the molecular organization of the neuron by
662 cryo-electron tomography. *Journal of Electron Microscopy*. 2011;60:137-48. doi:
663 10.1093/jmicro/dfr018. PubMed PMID: 21844585.
- 664 13. Siksou L, Rostaing P, Lechaire J-P, Boudier T, Ohtsuka T, Fejtova A, et al.
665 Three-Dimensional Architecture of Presynaptic Terminal Cytoarchitecture. *Journal of*
666 *Neuroscience*. 2007;27:6868-77. doi: 10.1523/JNEUROSCI.1773-07.2007.
667 PubMed PMID: 17596435.
- 668 14. Palade G. The fine structure of mitochondria. *The Anatomical record*.
669 1952;114:427-51. PubMed PMID: 12996882.
- 670 15. Frey TG, Mannella CA. The internal structure of mitochondria. *Trends Biochem*
671 *Sci*. 2000;25(7):319-24. PubMed PMID: 10871882.

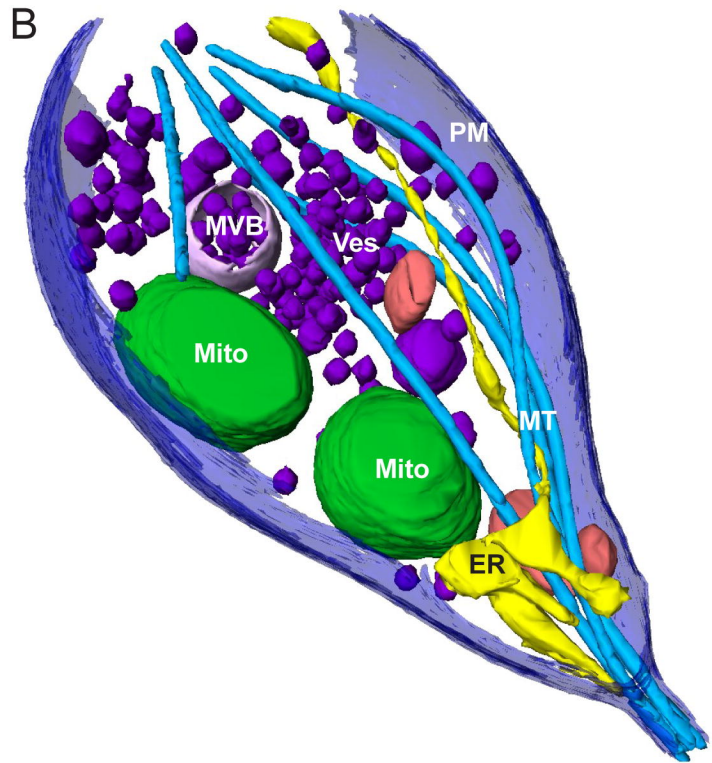
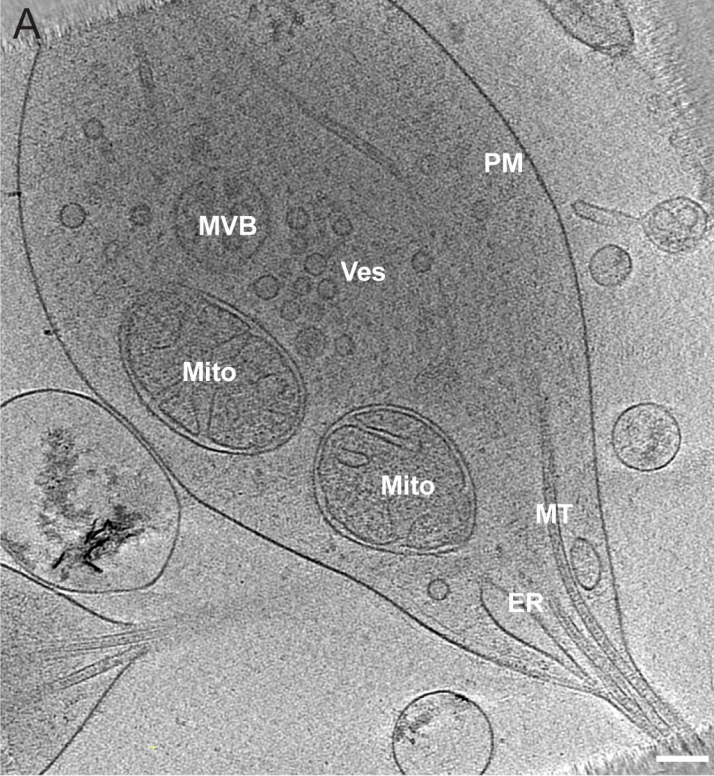
- 672 16. Rangaraju V, Calloway N, Ryan TA. Activity-driven local ATP synthesis is
673 required for synaptic function. *Cell*. 2014;156:825-35. doi:
674 10.1016/j.cell.2013.12.042. PubMed PMID: 24529383.
- 675 17. Devine MJ, Kittler JT. Mitochondria at the neuronal presynapse in health and
676 disease. *Nature Reviews Neuroscience*. 2018;19:63-80. doi:
677 10.1038/nrn.2017.170.
- 678 18. Sheng ZH. The Interplay of Axonal Energy Homeostasis and Mitochondrial
679 Trafficking and Anchoring. *Trends in Cell Biology*. 2017;27:403-16. doi:
680 10.1016/j.tcb.2017.01.005. PubMed PMID: 28228333.
- 681 19. Sun T, Qiao H, Pan PY, Chen Y, Sheng ZH. Motile axonal mitochondria
682 contribute to the variability of presynaptic strength. *Cell Reports*. 2013;4:413-9.
683 doi: 10.1016/j.celrep.2013.06.040. PubMed PMID: 23891000.
- 684 20. Li Z, Okamoto KI, Hayashi Y, Sheng M. The importance of dendritic mitochondria
685 in the morphogenesis and plasticity of spines and synapses. *Cell*. 2004;119:873-
686 87. doi: 10.1016/j.cell.2004.11.003. PubMed PMID: 15607982.
- 687 21. Wu Y, Whiteus C, Xu CS, Hayworth KJ, Weinberg RJ, Hess HF, et al. Contacts
688 between the endoplasmic reticulum and other membranes in neurons.
689 *Proceedings of the National Academy of Sciences*. 2017;114:E4859-E67. doi:
690 10.1073/pnas.1701078114. PubMed PMID: 28559323.
- 691 22. Chen X, Winters C, Azzam R, Li X, Galbraith JA, Leapman RD, et al.
692 Organization of the core structure of the postsynaptic density. *Proceedings of the*
693 *National Academy of Sciences*. 2008;105:4453-8. doi:
694 10.1073/pnas.0800897105. PubMed PMID: 18326622.
- 695 23. Grabrucker A, Vaida B, Bockmann J, Boeckers TM. Synaptogenesis of
696 hippocampal neurons in primary cell culture. *Cell Tissue Res*. 2009;338(3):333-
697 41. doi: 10.1007/s00441-009-0881-z. PubMed PMID: 19885679.
- 698 24. Hackenbrock CR, Caplan AI. Ion-induced ultrastructural transformations in
699 isolated mitochondria. The energized uptake of calcium. *J Cell Biol*.
700 1969;42(1):221-34. PubMed PMID: 5795884; PubMed Central PMCID:
701 PMC2107584.
- 702 25. Cogliati S, Enriquez JA, Scorrano L. Mitochondrial Cristae: Where Beauty Meets
703 Functionality. *Trends in Biochemical Sciences*. 2016;41:261-73. doi:
704 10.1016/j.tibs.2016.01.001. PubMed PMID: 26857402.
- 705 26. Cogliati S, Frezza C, Soriano ME, Varanita T, Quintana-Cabrera R, Corrado M,
706 et al. Mitochondrial cristae shape determines respiratory chain supercomplexes
707 assembly and respiratory efficiency. *Cell*. 2013;155:160-71. doi:
708 10.1016/j.cell.2013.08.032. PubMed PMID: 24055366.
- 709 27. Morris RL, Hollenbeck PJ. Axonal transport of mitochondria along microtubules
710 and F-actin in living vertebrate neurons. *Journal of Cell Biology*. 1995;131:1315-
711 26. doi: 10.1083/jcb.131.5.1315. PubMed PMID: 8522592.
- 712 28. Schwarz TL. Mitochondrial Trafficking in Neurons. *Cold Spring Harbor*
713 *Perspectives in Biology*. 2013:1-15. doi: 10.1101/cshperspect.a011304. PubMed
714 PMID: 23732472.
- 715 29. Sheng Z-H, Cai Q. Mitochondrial transport in neurons: impact on synaptic
716 homeostasis and neurodegeneration. *Nature reviews Neuroscience*. 2012;13:77-
717 93. doi: 10.1038/nrn3156. PubMed PMID: 22218207.
- 718 30. Vale RD, Hotani H. Formation of membrane networks in vitro by kinesin-driven
719 microtubule movement. *Journal of Cell Biology*. 1988;107:2233-41. doi:
720 10.1083/jcb.107.6.2233. PubMed PMID: 3143735.

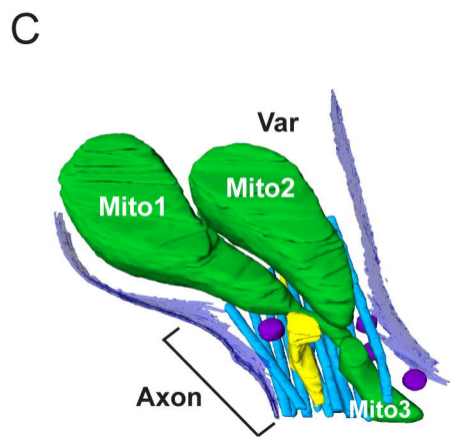
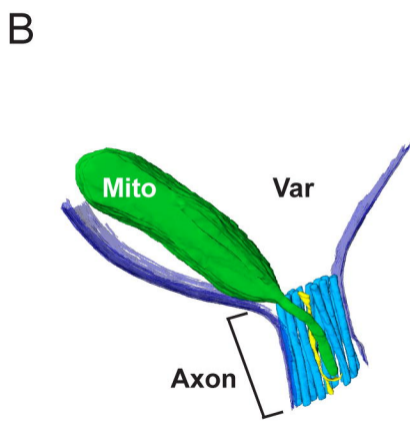
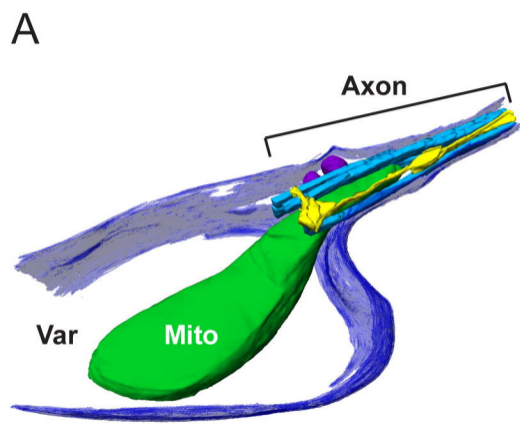
- 721 31. Vale RD, Reese TS, Sheetz MP. Identification of a novel force-generating
722 protein, kinesin, involved in microtubule-based motility. *Cell*. 1985;42:39-50. doi:
723 10.1016/S0092-8674(85)80099-4. PubMed PMID: 3926325.
- 724 32. Wang C, Du W, Su QP, Zhu M, Feng P, Li Y, et al. Dynamic tubulation of
725 mitochondria drives mitochondrial network formation. *Cell Research*.
726 2015;25:1108-20. doi: 10.1038/cr.2015.89. PubMed PMID: 26206315.
- 727 33. Helle SCJ, Feng Q, Aebersold MJ, Hirt L, Grüter RR, Vahid A, et al. Mechanical
728 force induces mitochondrial fission. *eLife*. 2017;6:e30292. doi:
729 10.7554/eLife.30292. PubMed PMID: 29119945.
- 730 34. Chereau R, Saraceno GE, Angibaud J, Cattaert D, Nagerl UV. Superresolution
731 imaging reveals activity-dependent plasticity of axon morphology linked to
732 changes in action potential conduction velocity. *Proc Natl Acad Sci U S A*.
733 2017;114(6):1401-6. doi: 10.1073/pnas.1607541114. PubMed PMID: 28115721;
734 PubMed Central PMCID: PMC5307438.
- 735 35. Pernas L, Scorrano L. Mito-Morphosis: Mitochondrial Fusion, Fission, and
736 Cristae Remodeling as Key Mediators of Cellular Function. *Annual review of*
737 *physiology*. 2015;78:annurev-physiol-021115-105011. doi: 10.1146/annurev-
738 *physiol-021115-105011*. PubMed PMID: 26667075.
- 739 36. Mannella Ca, Pfeiffer DR, Bradshaw PC, Moraru II, Slepchenko B, Loew LM, et
740 al. Topology of the mitochondrial inner membrane: dynamics and bioenergetic
741 implications. *IUBMB life*. 2001;52:93-100. doi: 10.1080/15216540152845885.
742 PubMed PMID: 11798041.
- 743 37. Davies KM, Anselmi C, Wittig I, Faraldo-Gomez JD, Kuhlbrandt W. Structure of
744 the yeast F1Fo-ATP synthase dimer and its role in shaping the mitochondrial
745 cristae. *Proceedings of the National Academy of Sciences*. 2012;109:13602-7.
746 doi: 10.1073/pnas.1204593109. PubMed PMID: 22864911.
- 747 38. Tarasenko D, Barbot M, Jans DC, Kroppen B, Sadowski B, Heim G, et al. The
748 MICOS component Mic60 displays a conserved membrane-bending activity that
749 is necessary for normal cristae morphology. *The Journal of Cell Biology*.
750 2017;216:889-99. doi: 10.1083/jcb.201609046. PubMed PMID: 28254827.
- 751 39. Mannella CA. Structure and dynamics of the mitochondrial inner membrane
752 cristae. *Biochimica et Biophysica Acta (BBA) - Molecular Cell Research*.
753 2006;1763:542-8. doi: 10.1016/j.bbamcr.2006.04.006. PubMed PMID: 16730811.
- 754 40. Hackenbrock CR. Ultrastructural bases for metabolically linked mechanical
755 activity in mitochondria. I. Reversible ultrastructural changes with change in
756 metabolic steady state in isolated liver mitochondria. *J Cell Biol*. 1966;30(2):269-
757 97. PubMed PMID: 5968972; PubMed Central PMCID: PMC2107001.
- 758 41. Hackenbrock CR. Ultrastructural bases for metabolically linked mechanical
759 activity in mitochondria. II. Electron transport-linked ultrastructural
760 transformations in mitochondria. *J Cell Biol*. 1968;37(2):345-69. PubMed PMID:
761 5656397; PubMed Central PMCID: PMC2107416.
- 762 42. Kühlbrandt W. Structure and function of mitochondrial membrane protein
763 complexes. *BMC biology*. 2015;13:89. doi: 10.1186/s12915-015-0201-x. PubMed
764 PMID: 26515107.
- 765 43. Friedman JR, Mourier A, Yamada J, Michael McCaffery J, Nunnari J. MICOS
766 coordinates with respiratory complexes and lipids to establish mitochondrial inner
767 membrane architecture. *eLife*. 2015;2015:1-61. doi: 10.7554/eLife.07739.
768 PubMed PMID: 25918844.
- 769 44. Harner ME, Unger AK, Geerts WJC, Mari M, Izawa T, Stenger M, et al. An
770 evidence based hypothesis on the existence of two pathways of mitochondrial

- 771 crista formation. *eLife*. 2016;5:1-25. doi: 10.7554/eLife.18853. PubMed PMID:
772 27849155.
- 773 45. Zerbes RM, Der Klei IJV, Veenhuis M, Pfanner N, Laan MVD, Bohnert M.
774 Mitofilin complexes: Conserved organizers of mitochondrial membrane
775 architecture. *Biological Chemistry*. 2012;393:1247-61. doi: 10.1515/hsz-2012-
776 0239. PubMed PMID: 23109542.
- 777 46. Chakrabarti R, Ji WK, Stan RV, Sanz JDJ, Ryan TA, Higgs HN. INF2-mediated
778 actin polymerization at the ER stimulates mitochondrial calcium uptake , inner
779 membrane constriction , and division. *Journal of Cell Biology*. 2018:1-18. doi:
780 10.1083/jcb.201709111. PubMed PMID: 29142021.
- 781 47. Cho B, Cho HM, Jo Y, Kim HD, Song M, Moon C, et al. Constriction of the
782 mitochondrial inner compartment is a priming event for mitochondrial division.
783 *Nature Communications*. 2017;8:15754. doi: 10.1038/ncomms15754. PubMed
784 PMID: 28598422.
- 785 48. Lee H, Yoon Y. Transient contraction of mitochondria induces depolarization
786 through the inner membrane dynamin opa1 protein. *Journal of Biological
787 Chemistry*. 2014;289:11862-72. doi: 10.1074/jbc.M113.533299. PubMed PMID:
788 24627489.
- 789 49. Misgeld T, Schwarz TL. Mitostasis in Neurons: Maintaining Mitochondria in an
790 Extended Cellular Architecture. *Neuron*. 2017;96:651-66. doi:
791 10.1016/j.neuron.2017.09.055. PubMed PMID: 29096078.
- 792 50. Verstreken P, Ly CV, Venken KJT, Koh T-W, Zhou Y, Bellen HJ. Synaptic
793 Mitochondria Are Critical for Mobilization of Reserve Pool Vesicles at *Drosophila*
794 Neuromuscular Junctions. *Neuron*. 2005;47:365-78. doi:
795 10.1016/j.neuron.2005.06.018. PubMed PMID: 16055061.
- 796 51. Pathak D, Berthet A, Nakamura K. Energy Failure : Does It Contribute to
797 Neurodegeneration ? 2013. doi: 10.1002/ana.24014.
- 798 52. Itoh K, Nakamura K, Iijima M, Sesaki H. Mitochondrial dynamics in
799 neurodegeneration. *Trends in Cell Biology*. 2013;23:64-71. doi:
800 10.1016/j.tcb.2012.10.006. PubMed PMID: 23159640.
- 801 53. Waxham MN, Aronowski J, Kelly PT. Functional analysis of Ca²⁺/calmodulin-
802 dependent protein kinase II expressed in bacteria. *J Biol Chem*.
803 1989;264(13):7477-82. PubMed PMID: 2496129.
- 804 54. Mastronarde DN. Automated electron microscope tomography using robust
805 prediction of specimen movements. *J Struct Biol*. 2005;152(1):36-51. doi:
806 10.1016/j.jsb.2005.07.007. PubMed PMID: 16182563.
- 807 55. Zheng SQ, Palovcak E, Armache JP, Verba KA, Cheng Y, Agard DA.
808 MotionCor2: anisotropic correction of beam-induced motion for improved cryo-
809 electron microscopy. *Nat Methods*. 2017;14(4):331-2. doi: 10.1038/nmeth.4193.
810 PubMed PMID: 28250466; PubMed Central PMCID: PMC5494038.
- 811 56. Kremer JR, Mastronarde DN, McIntosh JR. Computer visualization of three-
812 dimensional image data using IMOD. *J Struct Biol*. 1996;116(1):71-6. doi:
813 10.1006/jsbi.1996.0013. PubMed PMID: 8742726.
- 814 57. Mastronarde DN, Held SR. Automated tilt series alignment and tomographic
815 reconstruction in IMOD. *J Struct Biol*. 2017;197(2):102-13. doi:
816 10.1016/j.jsb.2016.07.011. PubMed PMID: 27444392; PubMed Central PMCID:
817 PMC5247408.
- 818 58. Agulleiro JI, Fernandez JJ. Fast tomographic reconstruction on multicore
819 computers. *Bioinformatics*. 2011;27(4):582-3. doi: 10.1093/bioinformatics/btq692.
820 PubMed PMID: 21172911.

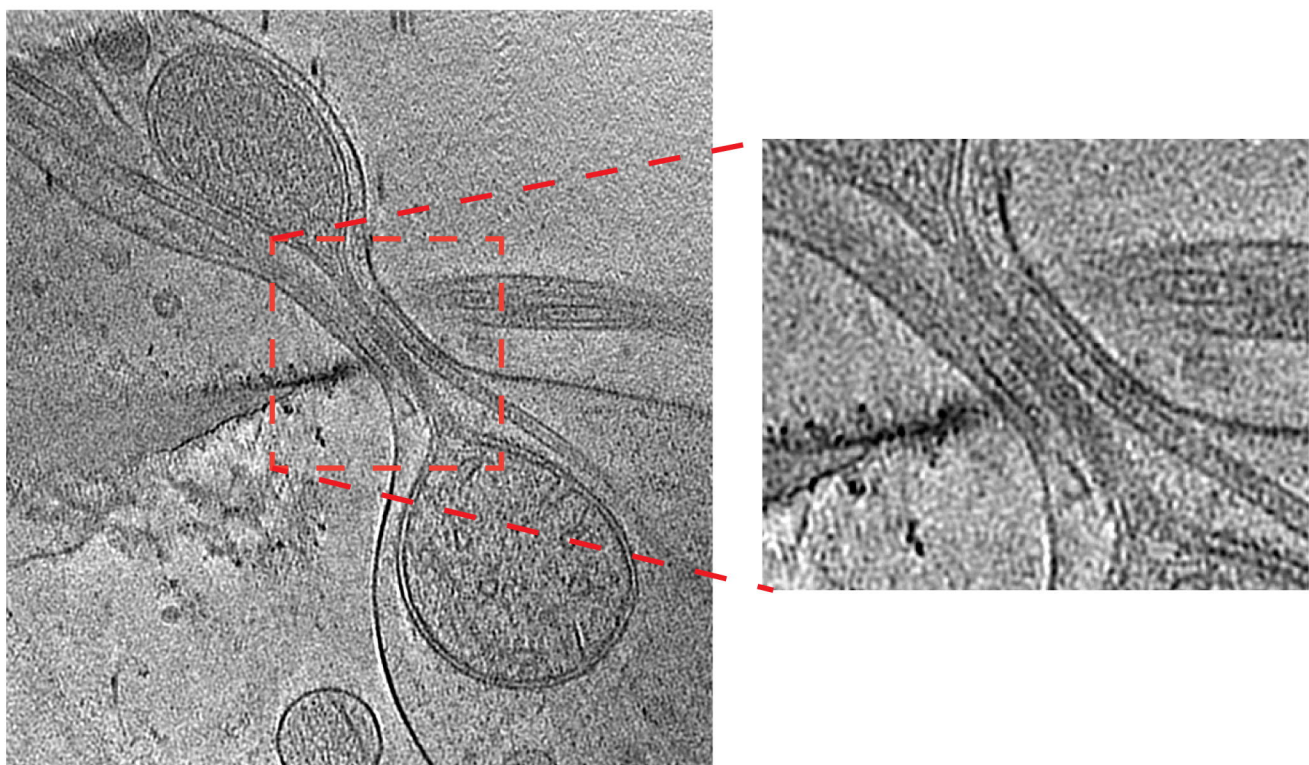
- 821 59. Agulleiro JI, Fernandez JJ. Tuning the cache memory usage in tomographic
822 reconstruction on standard computers with Advanced Vector eXtensions (AVX).
823 Data Brief. 2015;3:16-20. doi: 10.1016/j.dib.2014.12.010. PubMed PMID:
824 26217710; PubMed Central PMCID: PMC4509992.
825



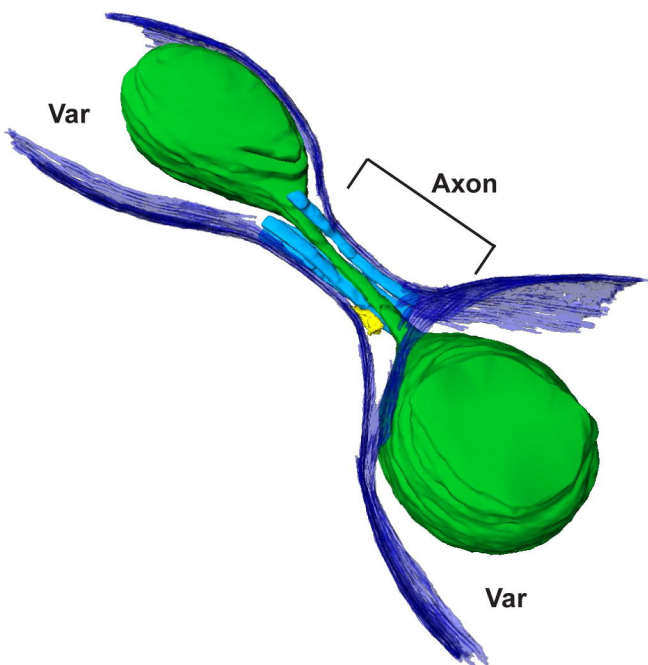




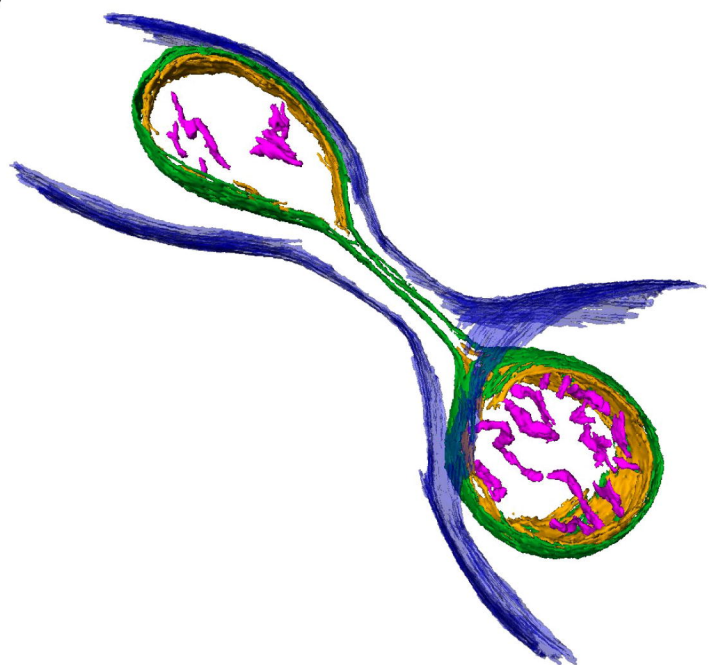
A



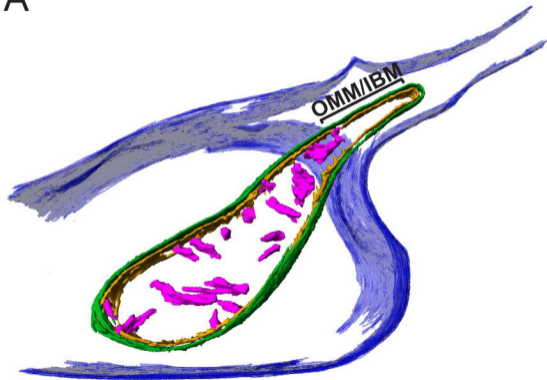
B



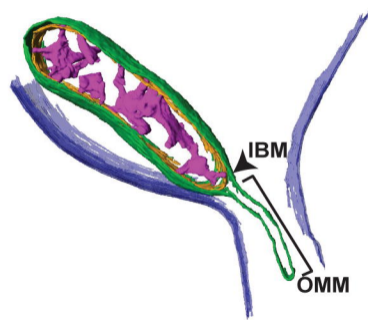
C



A



B



C

